



Title	Fatigue analysis of orthotropic steel-ultra-high-performance fiber-reinforced concrete (UHPFRC) composite deck considering accelerated deterioration and self-healing of fractured ultra-high-performance fiber-reinforced concrete in surface water condition
Author(s)	Ma, Chi Hieu; Deng, Pengru; Matsumoto, Takashi
Citation	Advances in Structural Engineering <a href="https://doi.org/10.1177/13694332231207180">https://doi.org/10.1177/13694332231207180</a>
Issue Date	2023-10-03
Doc URL	<a href="http://hdl.handle.net/2115/90625">http://hdl.handle.net/2115/90625</a>
Rights	Chi Hieu Ma, Pengru Deng, and Takashi Matsumoto, Fatigue analysis of orthotropic steel-ultra-high-performance fiber-reinforced concrete (UHPFRC) composite deck considering accelerated deterioration and self-healing of fractured ultra-high-performance fiber-reinforced concrete in surface water condition, Advances in Structural Engineering. Copyright © 2023. DOI: <a href="https://doi.org/10.1177/13694332231207180">https://doi.org/10.1177/13694332231207180</a>
Type	article (author version)
File Information	Final manuscript_T_Matsumoto_Adv_Struct_Eng_202310.pdf



[Instructions for use](#)

1           Fatigue analysis of orthotropic steel-UHPFRC composite deck  
2           considering accelerated deterioration and self-healing of fractured  
3           UHPFRC in surface water condition

4           Chi Hieu Ma<sup>a,\*</sup>, Pengru Deng<sup>c</sup> and Takashi Matsumoto<sup>b</sup>

5           <sup>a</sup>*Graduate School of Engineering, Division of Engineering and Policy for Sustainable Environment*  
6           *Hokkaido University, Kita-13, Nishi-8, Kita-ku, Sapporo 060-8628 Japan*

7           <sup>b</sup>*Faculty of Engineering, Division of Civil Engineering*

8           *Hokkaido University, Kita-13, Nishi-8, Kita-ku, Sapporo 060-8628 Japan*

9           <sup>c</sup>*School of Engineering, Central South University*

10          *No. 22, Shaoshan South Road, Tianxin District, Changsa City 410075 China*

11          Email address: [chihieuma@gmail.com](mailto:chihieuma@gmail.com), [pengrudeng@outlook.com](mailto:pengrudeng@outlook.com) and

12          [takashim@eng.hokudai.ac.jp](mailto:takashim@eng.hokudai.ac.jp); \*Corresponding author.

13          **Abstract**

14          In this study, an orthotropic steel bridge deck overlaid with ultra-high-performance fiber-reinforced  
15          concrete (UHPFRC) is investigated using the finite element analysis. The composite bridge deck  
16          which is undergone moving-wheel load is examined under environmental surface water conditions.  
17          Two phases, i.e., Phases 1 and 2, are considered for the material model of the UHPFRC with stagnant  
18          water. In Phase 1, mechanical recoveries of the tensile strength and reloading stiffness are considered  
19          for the cracked UHPFRC caused by the autogenous self-healing behavior. In Phase 2, under the  
20          moving-wheel load, the crack bridging stress degradation in reinforced overlayer accelerates due to  
21          the closing–opening actions of surface cracks in water. In both phases, the deformation behaviors of  
22          the steel deck plate and UHPFRC overlayer are numerically examined. The results of the current  
23          numerical model agree with the experimental data in terms of the strain tendency, wherein the strain

24 range of the steel deck plate and UHPFRC overlayer decreases in Phase 1 and progressively increases  
25 in Phase 2. Therefore, it can be asserted that, under the surface water condition, scenarios considering  
26 two phases of the material model of cracked UHPFRC, have governed the strain behaviors of the  
27 tested composite bridge deck.

28 **Key words:** UHPFRC, OSD, fatigue, crack bridging stress degradation, self-healing behavior, FEA

## 29 **1. Introduction**

30 In recent years, ultra-high-performance fiber-reinforced concrete (UHPFRC) with excellent  
31 properties, such as high tensile and compressive strengths and high fatigue durabilities, has been used  
32 to cover the top surfaces of orthotropic steel bridge decks (OSDs), creating a reinforcing layer to  
33 improve structural fatigue performance. Following such modifications, the overall stiffness of OSDs  
34 has been observed to increase, leading to remarkable reductions in fatigue stress levels in the steel  
35 members of the OSDs. Thus, the fatigue durability of OSDs can be improved with the application of  
36 UHPFRC overlayers (Dieng et al., 2013; Makino et al., 2021, Deng et al., 2021, Ma et al., 2021a, Mi,  
37 2020; Deng et al., 2022). It has been reported that, with such a thin thickness 25-mm of UHPFRC  
38 overlayer, the maximum magnitudes of displacement and stress level obtained in steel deck plate  
39 were notably reduced by over 37% and 88%, respectively (Makino et al., 2021).

40 However, for steel bridge decks covered by UHPFRC, stagnant water resulting from rainfall may  
41 adversely affect the structural performance of the reinforcing overlayer when subjected to repetitive  
42 traffic loading. Such stagnant water may pool over the UHPFRC, consequently subjecting the  
43 composite bridge deck to surface water conditions. Following this, the surface water may penetrate  
44 into microcracks on the top layer of the reinforced overlayer, further leading to severe fatigue  
45 deteriorations in the UHPFRC overlayer under moving-wheel loads. Matsui examined the effect of  
46 surface water on the structural performance of RC bridge decks (Matsui, 1987; Matsui, 1996). The  
47 results indicated that stagnant water on the top surface of RC bridge decks considerably degraded

48 their fatigue performance, and the fatigue life of the RC bridge decks reduced about 5% when the  
49 fatigue test was conducted under surface water condition (Matsui, 1996). Along similar lines, several  
50 experimental studies on the fatigue performance of concrete have been conducted in the presence of  
51 water, and the results have revealed that water adversely affects the fatigue durability of concrete  
52 materials (Waagaard, 1982; Solwik and Saouma, 2000; Matsushita, 1980; Maekawa and Fujiyama,  
53 2013). Under the rapid deformation of concrete cracks, i.e., the closing–opening actions of cracks  
54 under fatigue loading, a high pore water pressure can be induced owing to the dispersion of condensed  
55 water inside cracks (Solwik and Saouma, 2000). This may further rapidly deteriorate concrete  
56 materials when capillary pores are subjected to water pressure; these pores are often located at the  
57 vicinity of the aggregate/matrix interface (Maekawa and Fujiyama, 2013). According to Matsushita  
58 (Matsushita, 1980; Matsushita and Tokumitsu, 1979), when the applied minimum stress is zero, the  
59 stress range ratio  $S_r$  at 2,000,000 cycles for concrete with the presence of water is about 70% of that  
60 under dry conditions. Herein,  $S_r = \Delta\sigma / \sigma_{ult} = (\sigma_{max} - \sigma_{min}) / \sigma_{ult}$ ; where  $\sigma_{max}$  and  $\sigma_{min}$  are applied  
61 maximum and minimum stresses,  $\sigma_{ult}$  is limit stress of concrete material.

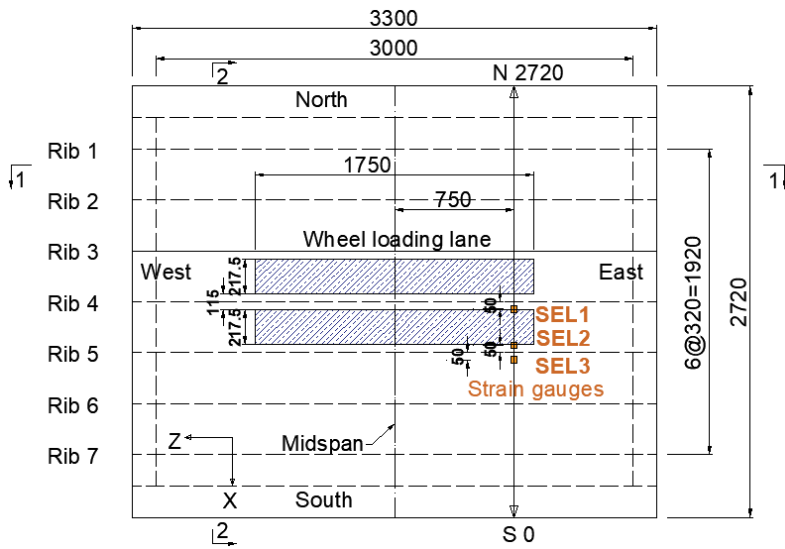
62 Without considering fatigue action of applied load, under water exposure, the self-healing  
63 capability of high-performance fiber-reinforced cement composites, such as engineered cementitious  
64 composite (ECC) and UHPFRC, with regard to crack closure and mechanical recovery has been  
65 previously investigated (Okuizumi et al., 2021; Herbert and Li, 2012, 2013; Zhang and Zhang, 2017;  
66 Li and Li, 2011; Kan and Shi, 2012; Kim et al., 2019; Cuenca and Serna, 2021). Owing to the low  
67 ratio of water to cement used in the design of ECCs or UHPFRC, extensive amounts of unhydrated  
68 cement grains may exist in the material matrix. Consequently, continued hydration of unreacted  
69 cement may occur at the fractured region in the presence of water, leading to the closure of cracks  
70 in the specimens under testing. In a study conducted by Okuizumi et al. (2021), UHPFRC was found  
71 to exhibit a high self-healing ability under water conditions based on a high crack closure rate, which  
72 was observed from the bottom section of UHPFRC beams that cracked owing to flexural loads. After

73 only 1 day of water exposure, the closure rate of the UHPFRC fine cracks within a width of 0.014  
74 mm in the specimens could reach over 77%. Herbert and Li (2012, 2013) examined the self-healing  
75 behavior of ECCs in the natural environment. Along with the closure of ECC cracks, mechanical  
76 recoveries of the tensile cracking strength and reloading stiffness in ECC specimens were observed  
77 after crack self-healing under water conditions. Moreover, under wet–dry cycles, the autogenous  
78 healing characteristics of high tensile ductility ECC materials were investigated by Kan and Shi  
79 (2012). The results revealed that the tensile strength and maximum tensile strain of the cracked  
80 specimens at the reloaded stage were higher than those of the reference specimens under dry  
81 conditions.

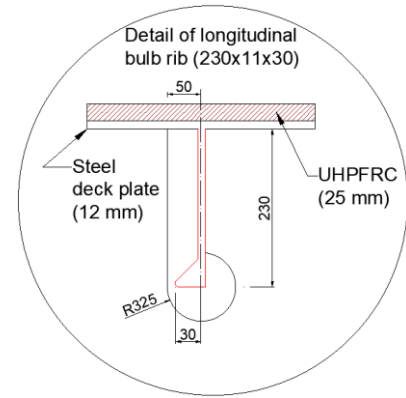
82 This paper proposes a numerical model based on the finite element method (FEM) to simulate an  
83 OSD overlaid by UHPFRC in the testing condition of surface water, and this deck is loaded by a  
84 moving rubber-tire wheel. Two phases of the material model considering the self-healing behavior  
85 and degradation in the fatigue life of cracked UHPFRC are introduced in this study. The proposed  
86 numerical model is validated using the experimental data reported by Makino et al., 2021. The  
87 structural responses from the considered phases, i.e., the deformation of steel members and the  
88 cracking behaviors of the reinforcing overlayer, are investigated in the analyses. The effect of self-  
89 healing behavior in UHPFRC cracks is also evaluated by a parametric study in the first phase.

## 90 **2. Testing conditions and considered phases for the material model of cracked UHPFRC**

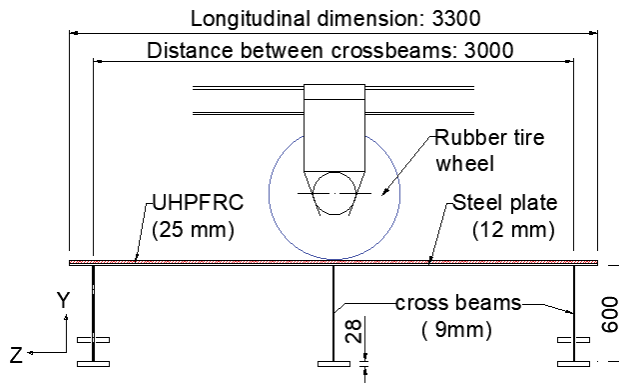
91 To examine the effectiveness of the UHPFRC overlayer in improving the fatigue life of an OSD,  
92 fatigue tests on a full-scale OSD were conducted under wheel loading and environmental conditions  
93 in the previous study (Makino et al., 2021). Fig. 1 illustrates the geometry of the investigated  
94 composite deck. The dimensions in transverse and longitudinal directions of the OSD were 2720 and  
95 3300 mm, respectively. The bridge deck comprised a 12 mm steel deck plate covered by a UHPFRC  
96 layer with a thickness of 25 mm, seven longitudinal ribs, three cross beams and two main girders.



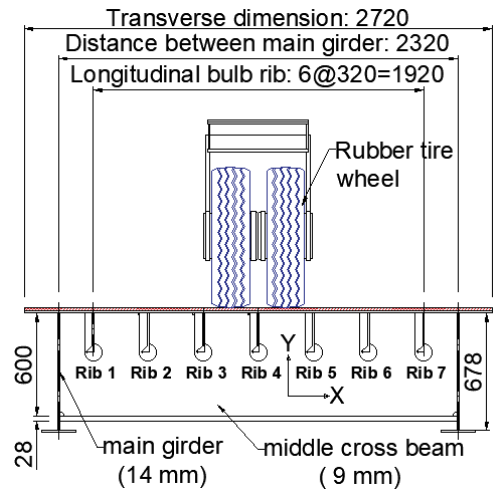
(a) Plan view



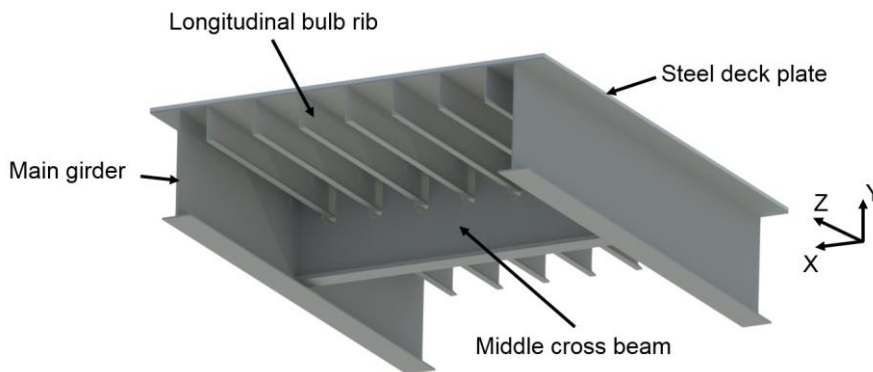
(b) Dimension of the longitudinal rib



(c) Side view (cross section 1-1)



(d) Front view (cross section 2-2)



(e) 3D view of the current OSD (excluding East and West cross-beams)

Fig. 1 The OSD geometry (all dimensions are in mm)

104 The web thicknesses of the main girders and crossbeams were 14 and 9 mm, respectively. The  
105 dimensions of the longitudinal bulb ribs were  $230 \times 11 \times 30 \text{ mm}^3$  (Fig. 1(b)).

106 The loading and environmental conditions adopted during the fatigue test for the composite bridge  
107 deck, and the fatigue test images of Stages 1 and 2 are depicted in Fig. 2. In the current study, fatigue  
108 analysis was conducted for Stage 2. After Stage 1, which included 1,100,000 cycles subjected to a  
109 moving wheel loaded with a rubber tire under dry conditions, the damaged composite deck with  
110 evident fine cracks on the top surface of the UHPFRC was subsequently tested for 60,000 cycles  
111 under the surface water condition in 1 day. For one night before the execution of Stage 2 of the fatigue  
112 test, a thin layer of water was deposited on the overlayer top surface. In the current fatigue analysis,  
113 two phases were considered for the material model of cracked UHPFRC.

114 - Phase 1: self-healing of cracked UHPFRC in water for one night from the 1,100,000th to the  
115 1,100,0001st loading cycle.

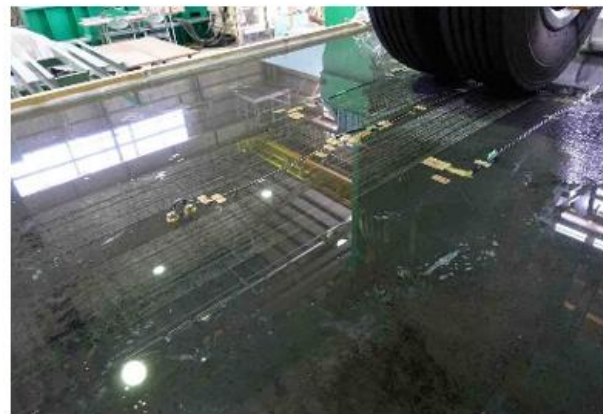
116 - Phase 2: higher degradation speed of cracked UHPFRC resulting from the combined action of  
117 fatigue wheel loading and surface water over 60,000 cycles.

118 The modeling of the behaviors for each phase of the cracked UHPFRC is detailed in Section 3.2.2.

Testing conditions for two consecutive stages [2]	Stage	Load level (kN)	Number of cycles	Loading condition	Environmental condition
	Stage 1	100	1,100,000	Rubber tire	Dry
	Stage 2	100	60,000	Rubber tire	Surface water



(a) Stage 1 (dry condition)



(b) Stage 2 (surface water condition)

119

120

Fig. 2 Fatigue test of the OSD (Makino et al., 2021)

121 **3. Method**

122 *3.1. Numerical model*

123 In this study, an OSD reinforced by UHPFRC overlayer undergone a moving load with a rubber  
 124 tire under the surface water condition is simulated utilizing the FEM software MSC/Marc. Using  
 125 Fortran programming language, a material user subroutine, which is applied to the Marc program to  
 126 solve nonstandard problems, is coded to define the cracking behaviors of the UHPFRC. In the defined  
 127 subroutine, the multi-fixed smeared crack model is applied to simulate crack initiation and  
 128 development in the UHPFRC (Rots and Blaauwendraad, 1989). In this crack model, the original  
 129 finite element mesh topology is maintained by transitioning from the initial isotropic stress-strain law



130 to an orthotropic relationship with the axes of orthotropy after the crack initiation. In other words, the  
 131 smeared crack model assumes a cracked body as a continuum, while the discrete crack approach  
 132 treats a crack as a discontinuous body with separated mesh elements. The initiation of UHPFRC  
 133 cracks is predicted based on the direction and magnitude of the maximum principal stress generated  
 134 in 3D UHPFRC eight-node elements. The first crack in the UHPFRC appears perpendicular to the  
 135 maximum principal stress direction if the tensile stress level approaches the tensile cracking strength  
 136 of the UHPFRC (i.e., value at point A in Fig. 4). Using a fixed crack model, the orientation of the  
 137 initial crack is maintained in the UHPFRC overlayer during the calculation process. With the  
 138 reorientation of the maximum principal stress when the wheel load moves, new cracks in the  
 139 UHPFRC element initiate along planes orthogonal to the initial crack plane; this occurs when the  
 140 cracking condition based on the maximum principal stress is satisfied.

141 Based on the procedure proposed by Rots and Blaauwendraad (1989), the overall stress–strain  
 142 relationship in the UHPFRC element can be obtained using the following equation:

$$143 \quad \sigma = D^{cocr} \varepsilon = \left[ D^{co} - D^{co} N (D^{cr} + N^T D^{co} N)^{-1} N^T D^{co} \right] \varepsilon, \quad (1)$$

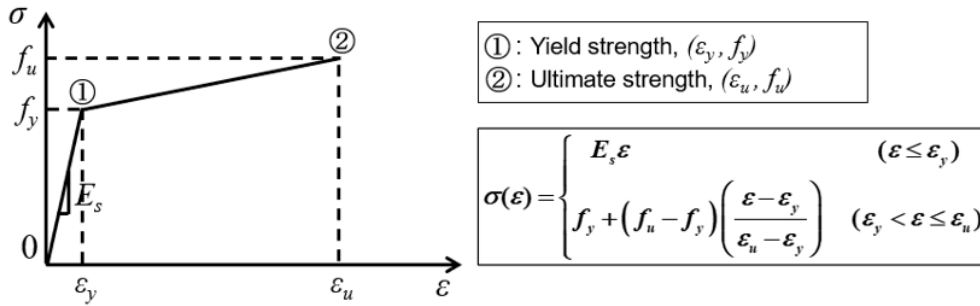
144 where  $\sigma$  and  $\varepsilon$  denote the global stress and strain vectors, including the elastic and cracked components,  
 145 respectively;  $D^{co}$  and  $D^{cr}$  denote the stiffness matrices of non-cracked and cracked components of the  
 146 UHPFRC, respectively;  $D^{cocr}$  denotes the overall stiffness matrix of the UHPFRC element;  $N$  denotes  
 147 the transformation matrix that defines crack orientation; and  $N^T$  denotes the transpose of matrix  $N$ .

## 148 3.2. Material model

### 149 3.2.1. Steel

150 The stress–strain relationship of the steel material, and the primary material properties of the steel  
 151 members are presented in Fig. 3. Notably, a Poisson’s ratio of 0.3 and Young’s modulus of 200 GPa  
 152 are considered in the current model. The von Mises criterion is used as the yield criterion of steel. In

153 the presence of the UHPFRC-strengthening layer, a significant decrease in stress levels was observed  
 154 from the fatigue sensitive locations of the OSD, and no fatigue cracking was observed from the steel  
 155 members. The fatigue of steel material was thus not prominent during the tested stages. In the current  
 156 analysis, the fatigue life of steel members is estimated in Phase 1 (as mentioned in Section 2) to assess  
 157 the beneficial effect of the self-healing behavior in UHPFRC cracks.



Material properties of steel	Steel members		Cross beam	Longitudinal rib	Steel plate
	Parameter				
Yield strength	$f_y$ (MPa)		245	365	365
Tensile strength	$f_u$ (MPa)		400	490	490
Ultimate tensile strain	$\epsilon_u$		0.22	0.23	0.23

158

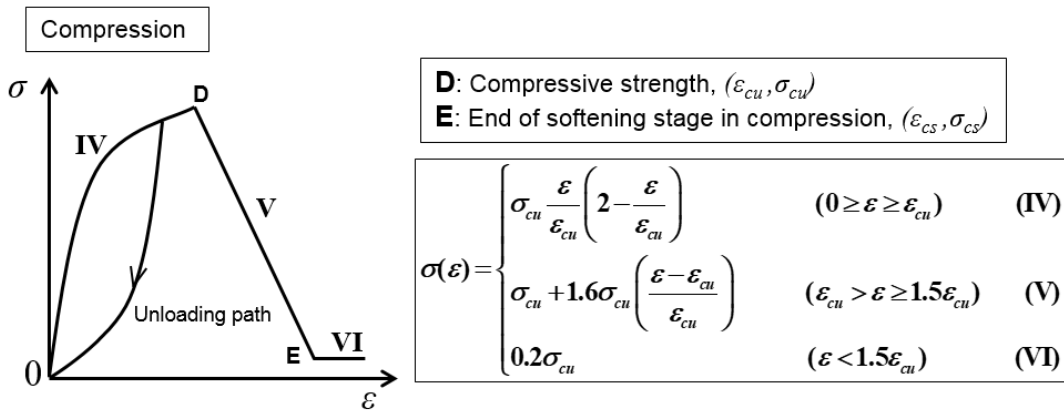
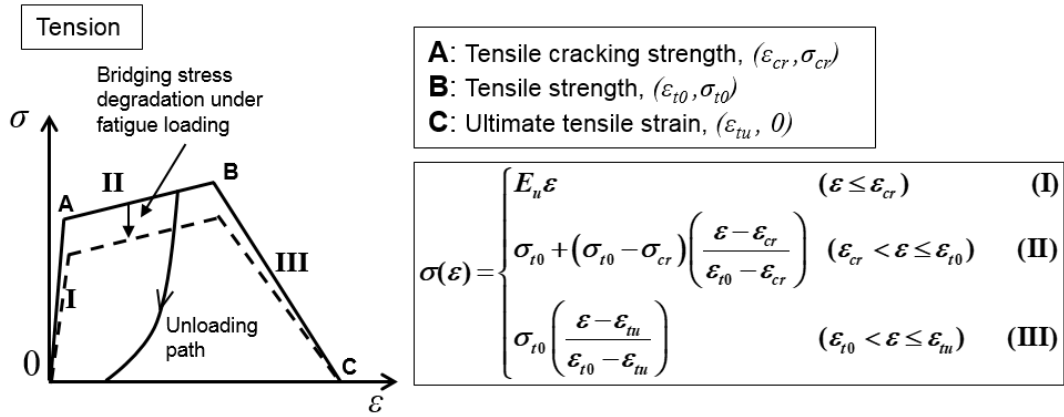
159

Fig. 3 Constitutive law and material properties of steel

160 3.2.2. UHPFRC

161 3.2.2.1. Nonlinear constitutive law of UHPFRC

162 A user subroutine in Marc program is coded to define the constitutive law of UHPFRC. According  
 163 to JSCE Recommendations (2008), the nonlinear stress–strain relationships of UHPFRC are  
 164 presented in Fig. 4. The constitutive law of UHPFRC under tension can be defined by a trilinear  
 165 relation, i.e., (I) elastic, (II) strain-hardening, and (III) strain-softening domains. After the elastic  
 166 domain, the tensile stress increases with the formation and propagation of microcracks in the second  
 167 domain, i.e., the strain-hardening domain. Following this, localized macrocracks initiate and develop  
 168 in the third domain after achieving the tensile strength.



169

Material properties of UHPFRC	Parameter	Notation	Value (unit)	Point
	Tensile cracking strength	$\epsilon_{cr}$		0.00019
	$\sigma_{cr}$		6 (MPa)	
Tensile strength	$\epsilon_{t0}$		0.00175	<b>B</b>
	$\sigma_{t0}$		9 (MPa)	
Ultimate tensile strain	$\epsilon_{tu}$		0.01200	<b>C</b>
Compressive strength	$\epsilon_{cu}$		0.0085	<b>D</b>
	$\sigma_{cu}$		133 (MPa)	
Ending point of compressive softening stage	$\epsilon_{cs}$		0.01275	<b>E</b>
	$\sigma_{cs}$		26.6 (MPa)	

170

Fig. 4 Nonlinear stress–strain relationships and material properties of UHPFRC

171

The constitutive law of UHPFRC under compression can be defined by a parabolic relation in the

172

(IV) fourth domain. When the compressive strength is reached, a linearly descending relation

173

representing the softening law is used in the (V) fifth domain. Subsequently, the compressive stress

174

presents a plateau at the end of the softening stage in the (VI) final domain.

175 For the elastic state, a Young's modulus ( $E_u$ ) of 31.3 GPa and Poisson's ratio ( $\nu$ ) of 0.22 were used  
 176 in the analysis, following the in-site uniaxial compressive test of UHPFRC. The material properties  
 177 referring to the UHPFRC material pamphlet provided by J-THIFCOM Construction Association  
 178 (2020) are employed this study and summed in the embedded table in Fig. 4.

179 For shear stress transfer in the UHPFRC after the occurrence of tensile cracks, the progressive  
 180 reduction in shear stiffness with an increase of tensile strain is considered in the current model  
 181 (Fairbairn et al., 2006). A shear retention factor  $\lambda$  which is a function of the maximum tensile strain  
 182  $\varepsilon_{tmax}$  is introduced in the analysis.

$$183 \quad \lambda = \frac{1}{1 + 4447\varepsilon_{tmax}} \quad (2)$$

#### 184 3.2.2.2. Self-healing behavior of the cracked UHPFRC under surface water conditions

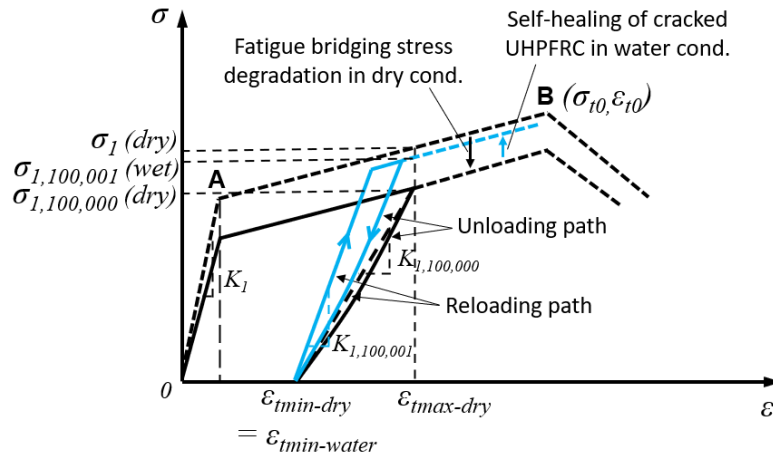
185 Based on the studies conducted by Herbert and Li (2012, 2013), the mechanical recoveries of  
 186 tensile strength and reloading stiffness of the UHPFRC surface cracks are considered in the current  
 187 analysis, from the end stage of the dry condition (1,100,000th cycle) to the beginning stage of the  
 188 surface water condition (1,100,001st cycle) in Phase 1 (Fig. 5).

189 The recovery ratios of the tensile strength,  $\xi$ , and reloading stiffness,  $\kappa$ , in the overlayer surface  
 190 cracks are defined as follows:

$$191 \quad \xi = \frac{\sigma_{1,100,001} - \sigma_{1,100,000}}{\sigma_1 - \sigma_{1,100,000}}, \quad (3)$$

$$192 \quad \kappa = \frac{K_{1,100,001} - K_{1,100,000}}{K_1 - K_{1,100,000}}, \quad (4)$$

193 Where  $\sigma_1$ ,  $\sigma_{1,100,000}$ , and  $\sigma_{1,100,001}$  denote the crack bridging stresses at the 1st, 1,100,000th, and  
 194 1,100,001st cycles, respectively;  $K_1$ ,  $K_{1,100,000}$  and  $K_{1,100,001}$  denote the reloading stiffnesses at the  
 195 1st, 1,100,000th and 1,100,001st cycles, respectively.



196

197 Fig. 5 Tensile stress–strain relation of the cracked UHPFRC under the surface water condition

198 The mechanical recoveries, especially for tensile strength, of the cracked UHPFRC under surface  
 199 water condition are meaningful for the current fatigue test of Stage 2. By reducing the maximum  
 200 tensile strain  $\varepsilon_{max}$  of UHPFRC cracks after self-healing, the bridging stress degradation can thus be  
 201 decelerated during fatigue loading, as referred to the Eqs. (5) - (6) in the next section.

202 Since the exposure time of the UHPFRC top layer in water is one night before the fatigue loading  
 203 test, the tensile strength and reloading stiffness recovery ratios in this study are roughly chosen as  
 204 70%,  $\kappa = \xi = 70\%$ , following the observations from the research of Okuizumi et al. (2021).

205 *3.2.2.3. Fatigue degradation of UHPFRC crack bridging stress under the condition of surface water*

206 Under fatigue loading, the primary factor influencing crack development in various cement-based  
 207 composites can be attributed to the gradual decrease in bridging stress between crack surfaces, which  
 208 results from fatigue deterioration of tensioned fibers, i.e., fiber rupture or pullout (Li and Matsumoto,  
 209 1998; Matsumoto and Li, 1999; Zhang et al., 1999, 2000; Suthiwarapirak et al., 2004; Deng and  
 210 Matsumoto, 2018; Jimi et al., 2021). For the UHPFRC, based on the study conducted by Jimi et al.  
 211 (2021), the degradation law for the crack bridging stress under dry conditions is adopted in the current  
 212 model for Stage 1 and is expressed as following equation:

213 
$$\frac{\sigma_N}{\sigma_1} = 1 - (0.015 + 5\varepsilon_{t,\max}) \log(N) \quad (5)$$

for  $1 \leq N \leq 1,100,000$

214 where  $\sigma_N/\sigma_1$  denotes the ratio of bridging stress degradation from  $N$ th to 1st cycles under dry condition.

215 According to researches of Matsushita (1980) for concrete material, when the applied minimum  
 216 stress is zero, the ratio of fatigue stress range at 2,000,000 cycles with the presence of water is about  
 217 70% of that under the dry condition. In the current study, by considering this reduced percentage from  
 218 the fatigue life of the concrete material to that of the UHPFRC, the corresponding degradation relation  
 219 of bridging stress for the overlayer cracks under the surface water condition is established and applied  
 220 in Phase 2.

221 
$$\frac{\sigma_N}{\sigma_{1,100,001}} = 1 - (0.058 + 3.5\varepsilon_{t,\max}) \log(N - 1,100,000) \quad (6)$$

for  $1,100,001 \leq N \leq 1,160,000$

222 where  $\sigma_N/\sigma_{1,100,001}$  denotes the ratio of bridging stress degradation from  $N$ th to 1,100,001st cycles  
 223 under the condition of surface water.

#### 224 **4. Interfacial fatigue degradation between steel plate and UHPFRC**

225 In the current fatigue test, the UHPFRC overlayer was cast in place. Before applying the UHPFRC  
 226 layer, the shot blasting was used as a surface treatment technique to remove the contamination on the  
 227 surface of steel deck plate. After placing the epoxy bonding agent on steel deck plate with average  
 228 thickness of 1 mm, hard aggregates (i.e., synthetic ceramics) with a grain size of up to 2 mm were  
 229 distributed over the top surface of bonding agent to increase the surface roughness (Fig. 6(a)).  
 230 UHPFRC was then casted within the available time of epoxy bonding agent (i.e., within 5 minutes in  
 231 20°C room temperature). According to the pull-off tensile test of composite specimens, the average  
 232 tensile bond strength of the current bonding technique was up to 2.91 MPa. For the epoxy resin  
 233 material at the interface between UHPFRC overlayer and steel plate, a linear elastic shear stress–

234 strain relationship is assumed in the current analysis (Fig. 6(a)). The shear elastic stiffness of the bond  
 235 material, i.e.,  $E_{b1}$ , is 2.66 GPa, is used following properties reported by Mitamura et al. (2011). In  
 236 fatigue analysis of Stage 1, the interfacial bond stiffness degradation between steel plate and overlayer  
 237 caused by repetitive moving-wheel load (see Fig. 6(a)) was considered by Ma et al. (2021). According  
 238 to this study, by comparing the experimental observations (i.e., steel strain and hammer tapping test  
 239 results) with the analysis results, the bond stiffness degradation speed was determined, as follows:

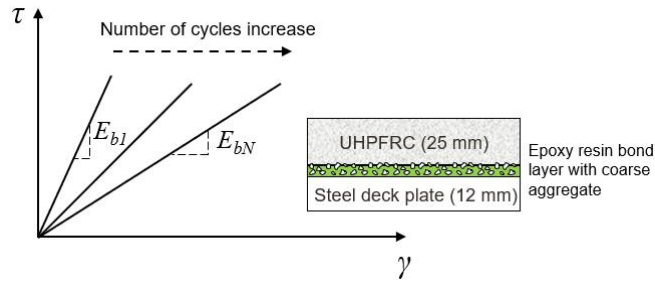
$$240 \quad \frac{E_{bN}}{E_{b1}} = f(N) = 1 - 0.1707 \times \log(N) \quad (7)$$

for  $1 \leq N \leq 700,000$

241 where  $E_{bN}/E_{b1}$  denotes the ratio of the interfacial stiffness from  $N$ th to 1st cycles. The region being  
 242 applied the bond stiffness degradation,  $S = 2 \times 302 \times 1875 \text{ mm}^2$ , is shown in Fig. 6(c.I).

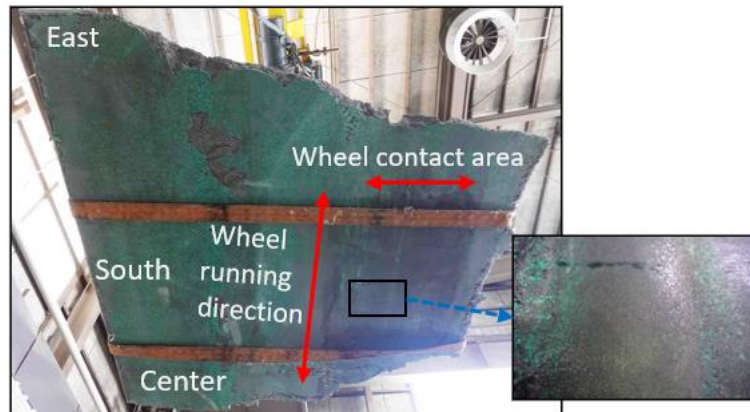
243 Subsequently, the delamination area at the interface was considered for the FEM model from the  
 244 700,000th cycle when the interfacial bond stiffness under wheel load region was zero (Ma et al.,  
 245 2021). Fig. 6(b) shows the bonding layer at the UHPFRC/steel interface at the end of the experiment.  
 246 The dark region under the wheel contact area, which comprised iron oxide particles obtained from  
 247 shot-blasting process for the steel plate before applying the UHPFRC overlayer, could be observed  
 248 after the fatigue test. This denoted the fatigue failure of bonding layer at wheel load region. In addition,  
 249 based on acoustic inspections, i.e., a hammer test, in Stage 1 (see Fig. 6(c)), the abnormal noise range  
 250 was detected at the 760,000th cycle, indicating the occurrence of interfacial delamination. Thereafter,  
 251 the delamination area found by the hammer test gradually expanded in the local region above Rib 5.  
 252 For the current model, the delamination area at the interface chosen at the initiating cycle of Stage 2  
 253 (1,100,001st) was equal to that at the ending cycle of Stage 1 (1,000,000th), as shown in Fig. 6(c.II).  
 254 Throughout Stage 2, the average expansion speed of 4.67 mm/10,000 cycles along the transverse  
 255 direction, which was applied to the interfacial debonded area, was selected identical to that of the

256 previous cycles in Stage 1 (from the 940,000th to the 1,100,000th cycles). The transverse dimension  
 257 of the debonded area are then gradually increased from 840 to 868 mm (Fig. 6(c.III)).



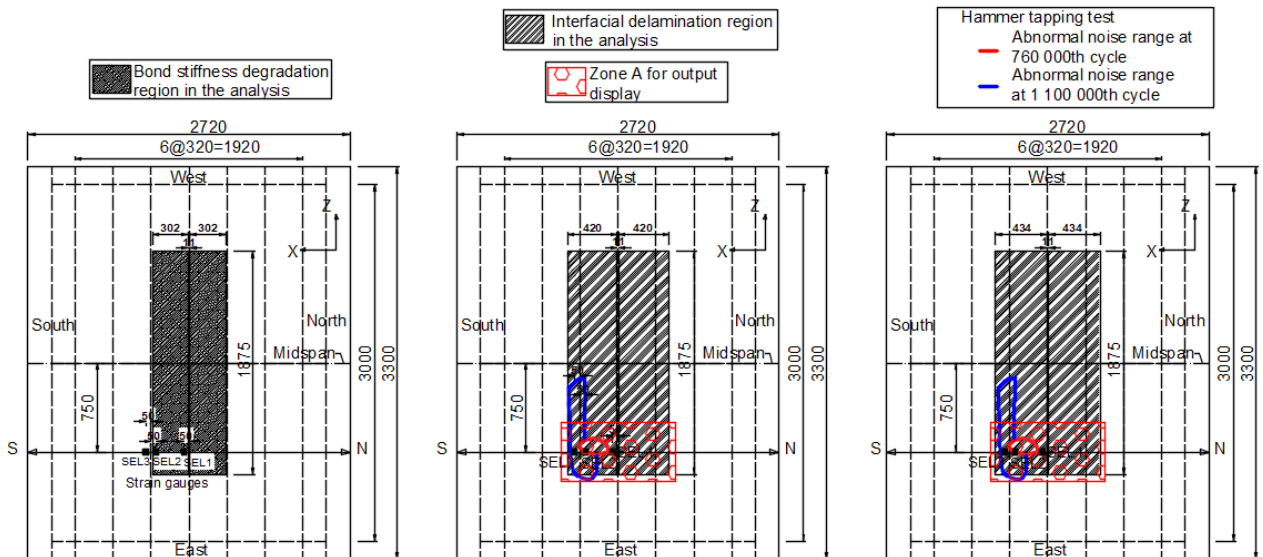
258

259 (a) Bond stiffness degradation model at steel/UHPFRC interface (Ma et al., 2021).



260

261 (b) Interfacial bond layer at the end of fatigue test (Makino et al., 2021).



262

263 (c.I) Before 700,000 cycle      (c.II) At 1,100,001st cycle      (c.III) At 1,160,0010th cycle

264 (c) Interfacial degradation areas for fatigue analysis of Stage 2 (All dimensions are in mm)

265

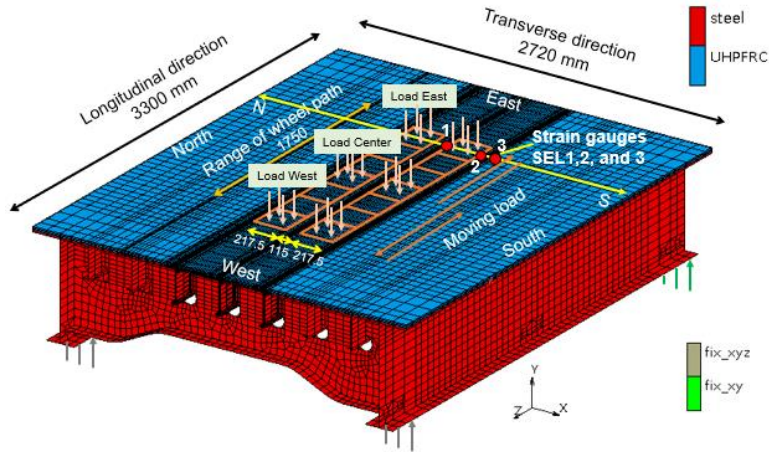
Fig. 6 Interfacial degradation model in the fatigue analysis



## 266 **5. Finite element modeling of the composite bridge deck**

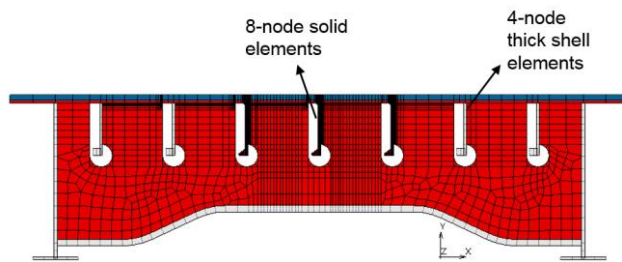
267 The boundary conditions and mesh pattern in the FEM model of the composite deck are shown in  
268 Fig. 7(a). Notably, a fine mesh with a minimum transverse size of 2.5 mm was employed for the  
269 overlayer and steel plate at regions above the three central longitudinal ribs. The UHPFRC-reinforced  
270 layer was vertically segregated into three layers in the current FEM model. In order to minimize  
271 computational cost, the 4-node thick shell elements are utilized instead of the 8-node solid elements  
272 to model the steel members such as cross beams, main girders, and the 4 outer bulb ribs (which are  
273 located far away from the critical region at wheel loading lane, as shown in Fig. 7(b)). It was found  
274 that, in comparison the model using only solid elements, the analysis time of the current model  
275 reduced about 40%, while the differences between numerical results at critical locations in steel deck  
276 plate of the two FE model are within 1%. The total number of elements used in the current FE model  
277 are 47,390.

278 Four edges under the main girders were supported with a 3000 mm longitudinal span. Two edges  
279 along the west side were restricted in all the three translational directions. The other edges from the  
280 east side were constrained against translation along the X and Y directions. The rubber tire wheel  
281 with a load of 100 kN was simulated using seven load locations. The size of each load location was  
282  $2 \times 217.5 \times 250 \text{ mm}^2$ , with a central gap of 115 mm, i.e., the distance between two tires. The 100-kN  
283 wheel-load was distributed over the whole area of load location, in which non-uniform distributions  
284 along the longitudinal and transverse directions of contact patch of rubber tire were based on the  
285 loading model presented by Ma et al. (2021), which has been reported to provide a better prediction  
286 of structural responses in steel deck plate than the standard uniformly-distributed load model. To  
287 simulate the interface between UHPFRC and steel plate in FEM model, the UHPFRC bottom layer  
288 and the steel-plate top surface are designated as deformable bodies of the contact analysis in  
289 MSC/Marc. The Touching contact option is used to model the interfacial delamination region (see  
290 Fig.6(c)), in which the material penetration is prevented. The remain interfacial region is simulated



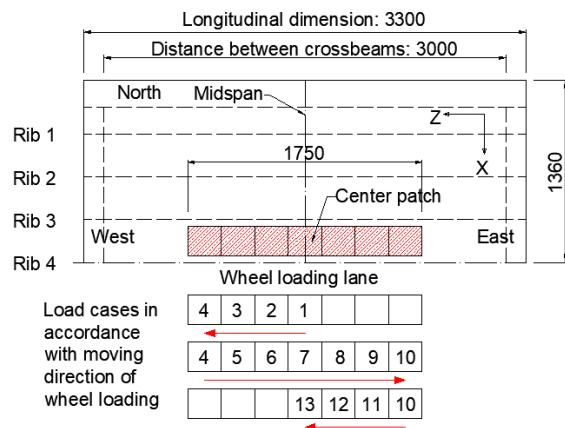
291  
292

(a) Boundary conditions



293  
294

(b) Front view of FEM model



295  
296

(c) Moving direction and load cases used in a single cycle

297

Fig. 7 FEM model of the composite deck (All dimensions are in mm)

298 by the Glue contact option, in which the interfacial contact stiffness between the deformable bodies  
299 is assigned to be the elastic modulus  $E_{bl}$  of UHPCFRC.

300 In the fatigue analysis, the moving direction of wheel loading under the specified load cases in a  
301 single cycle is presented in Fig. 7(c). The wheel load is initially applied to the central location until

302 the peak value (100 kN) is reached from load case 1. In load case 2, this location is unloaded with the  
303 loading of the adjacent elements at the same increasing rate. Herein, each load case includes 30  
304 loading steps with a total running time of 2190s. This procedure is continuously repeated along the  
305 loading lane, reproducing the movement of the rubber tire wheel. During this process, the bridging  
306 stress degradation equation (i.e., Eq. (6)) and unloading behaviors at each integration point of the  
307 UHPFRC elements are modified and determined based on the maximum value of tensile strain, which  
308 is recorded from the previous cycle of the fatigue analysis. The obtained bridging stress degradation  
309 value at each node is then applied directly to the nonlinear constitutive law of UHPFRC after cracking  
310 which is defined in the multi-fixed smeared crack model for each cycle. The current analysis of Stage  
311 2 is performed for 60,000 cycles to reproduce the fatigue test under surface water condition.

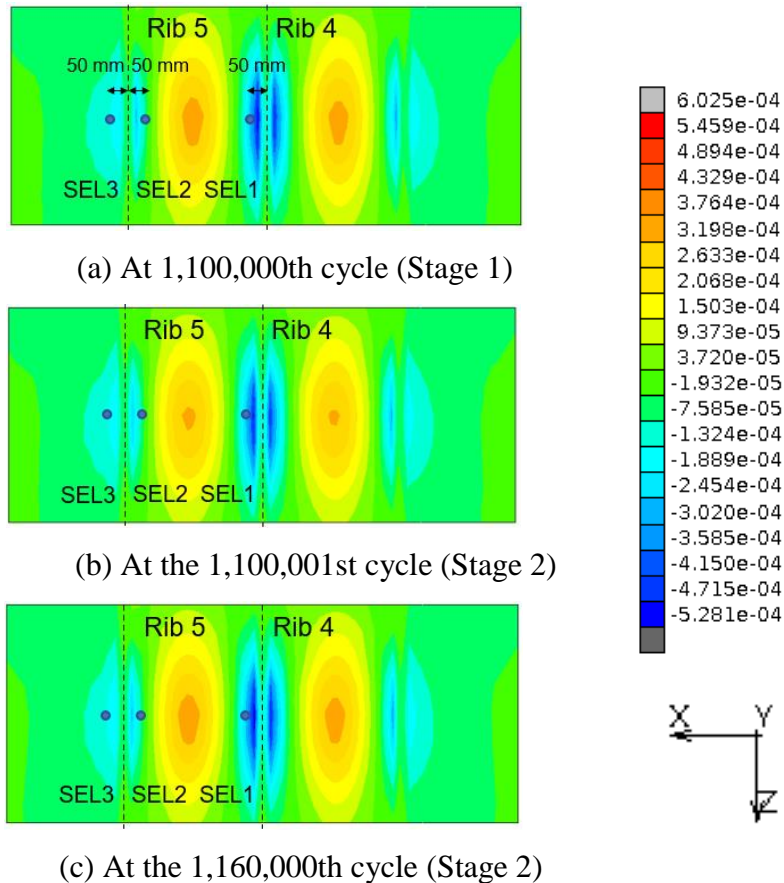
## 312 **6. Results and discussions**

### 313 *6.1. Steel strains in the deck plate*

#### 314 *6.1.1 Numerical steel strain distributions*

315 The distributions of the transverse strain under bottom surface of the steel deck plate for different  
316 cycles are depicted in Fig. 8. The illustrated results are obtained from zone A (Fig. 6(c.II)) under load  
317 case 10. Under load case 10, the positive bending at the tire contact region is produced by the wheel  
318 load along with the overall downward movement of the steel deck plate. On the other hand, owing to  
319 the stiffening effect of the longitudinal Ribs 3,4 and 5, the wheel load induces negative bending at  
320 these local regions. At the 1,100,001st cycle (Phase 1), owing to an increase in the tensile strength of  
321 the fine cracks in the UHPFRC overlayer after autogenous self-healing (Section 3.2.2), the overall  
322 stiffness of the composite deck increases after one-night exposure to water. This leads to a decrease  
323 in strain levels in the compressive zones at Ribs 3–5 and tensile zones at the wheel contact area of  
324 the steel deck plate during this loading cycle. Further, the mechanical recoveries of the cracked  
325 UHPFRC in Phase 1 can be interpreted based on the opening–closing actions of a single crack (Fig.

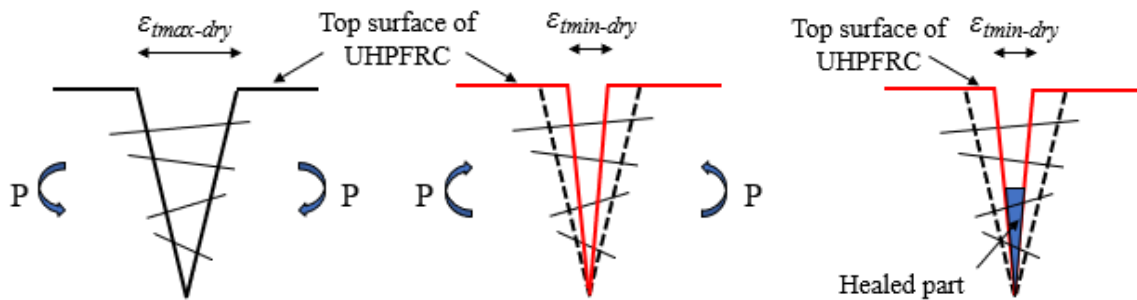
326 9) on the top layer of the overlayer before and after self-healing. It is noted that the UHPFRC tensile  
 327 cracks at East patch above Ribs 3, 4 and 5 are under the process from opening to closing when the  
 328 wheel load moves from East to West load patches; and vice versa. In the presence of the healed part  
 329 inside the UHPFRC crack, the stress transfer between pulled-out or ruptured fibers is restored,  
 330 causing an increase in the bridging stress between the crack surfaces. Thus, the reloaded maximum  
 331 strain or crack opening displacement decreases after the self-healing of UHPFRC cracks (Fig. 9(d)).  
 332 The autogenous healing process of the UHPFRC cracks is assumed to terminate at the beginning of  
 333 the 1,100,001st cycle (Fig. 9(c)), and the healed parts undergo cracking and degradation under  
 334 repetitive wheel loading without further self-healing throughout Stage 2. Therefore, the unloading



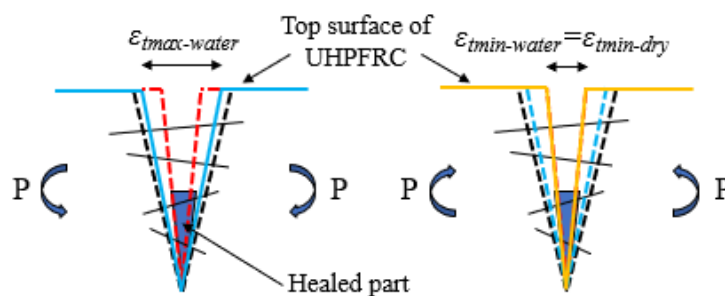
341 Fig. 8 Distributions of the steel transverse strain under bottom surface of the deck plate for different  
 342 cycles in load case 10 (displayed at zone A).

343 minimum strain under the water condition ( $\epsilon_{tmin-water}$ ) is maintained equal to that under the dry  
 344 condition ( $\epsilon_{tmin-dry}$ ) (Fig. 9(e)).

345 In contrast to the first cycle of Stage 2, the increase in transverse strain magnitudes can be observed  
 346 at the 1,160,000th cycle (see Fig. 8(c)), and this is owing to fatigue bridging stress degradation of  
 347 cracked UHPFRC under moving-wheel loading in Phase 2. After the formation of a tensile crack,  
 348 owing to the continuous reduction in tensile strength resulting from the degradation in the bridging  
 349 stress between crack surfaces, a stress concentration can be induced in the region of the crack tip.  
 350 Thereafter, the fatigue crack propagates in the overlayer with a newly formed crack length at the  
 351 crack tip. Consequently, the deformation of the bridge deck is increased, leading to strain  
 352 redistribution in the UHPFRC and steel plate. Moreover, stiffness reduction of the bridge deck is as



353  
 354 (a) Loading under dry condition (b) Unloading under dry condition (c) Healed part formed inside  
 355 crack



356  
 357 (d) Reloading under water condition (e) Unloading under water condition

358 Fig. 9 Opening–closing behaviors of a UHPFRC crack before (a and b) and after (d and e) self-  
 359 healing.

360 well due to the expansion of the debonded area at steel/UHPFRC interface, which leads to a  
361 progressive loss in the capability of shear force transfer between the overlayer and steel plate. The  
362 degradation in crack bridging stress of UHPFRC, which are dependent on the maximum level of the  
363 tensile strain, is thus accelerated, along with the interfacial–delamination development. As a result,  
364 those kinds of fatigue degradations with their mutual interaction can considerably deteriorate the  
365 structural performance of the tested bridge deck.

### 366 *6.1.2 Numerical and experimental steel strain evolutions*

367 In Fig. 10, the transverse strain range evolutions in load case 10 at the locations of the SEL strain  
368 gauges (Fig. 1(a)) under steel-plate bottom are plotted in comparison with the experimental data, with  
369 the chosen recovery ratios for tensile strength and reloading stiffness of 70%. As reported by Ma et  
370 al. (2021), in Stage 1, owing to continuous deterioration of the interfacial bond stiffness before the  
371 700,000th cycle, the strain range of the steel deck plate gradually decreases with an increase of the  
372 number of cycles. Subsequently, a delamination area formed at the UHPFRC/steel interface and  
373 expands along the transverse direction, leading to considerable variations in the transverse strain  
374 range levels of the steel deck plate from 700,000th to 1,100,000th cycles. From Fig. 10, it is apparent  
375 that the experimental strain range magnitudes at the SEL strain gauges from the end of Stage 1  
376 (1,100,000th cycle) to the beginning of Stage 2 (1,100,001st cycle) have decreased after one-night  
377 exposure in surface water condition. Possible cause of this behavior is the self-healing of surface  
378 cracks in the overlayer, as introduced above. To assess the effect of this mechanism on the structural  
379 responses of the composite deck, a parametric study is conducted and presented in the following  
380 section.

#### 381 *6.1.2.1 Effect of self-healing behaviors on strain responses in Phase 1*

382 Based on the current analysis under surface water condition in Phase 1, Fig. 11 shows the  
383 relationships between the recovery ratios of tensile strength and reloading stiffness caused by self-

384 healing, along with the results of the transverse strain range considering the reduction rates from the  
 385 1,100,001st cycle at strain gauge SEL1, i.e., steel plate's critical location. When the recovery ratios  
 386 after the self-healing of UHPFRC cracks increase, the transverse strain range levels at SEL1 decrease,  
 387 along with an increase in the reduction rates of the strain range. In the current model, with recovery  
 388 ratios of 100% for the UHPFRC surface cracks, the reduction in the transverse strain range at SEL1  
 389 can reach 7.32% (reduced from -267.7 $\mu$  to -248.1 $\mu$ ). Based on the Japan Society of Steel Construction  
 390 (JSSC) code (1993), the prediction analysis of the fatigue life at the critical point of SEL1 is  
 391 conducted using the obtained transverse strain ranges. The fatigue life (in years) ( $N$ ) is calculated as  
 392 follows:

$$393 \quad N = \frac{n \times 100}{n_{i-100}}$$

394 where  $n = \frac{(FAT)^m \times (2 \times 10^6)}{\Delta\sigma_{eq}^m}$  is the number of cycles causing fatigue cracks; here,  $FAT = 80$  MPa

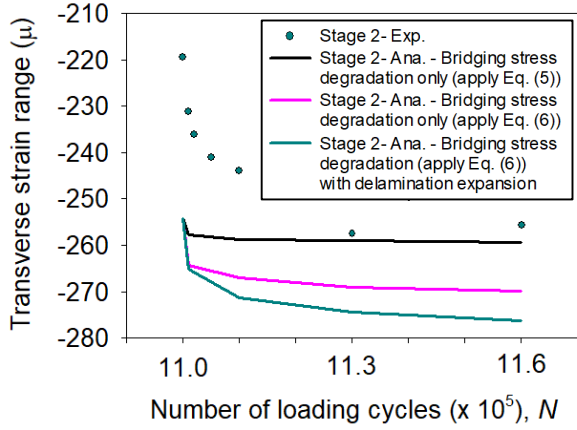
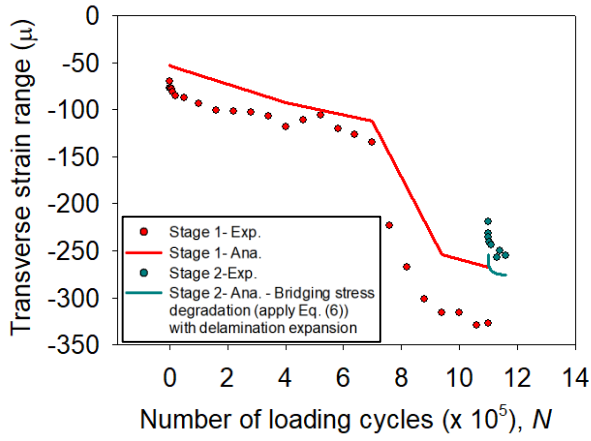
395 and  $m = 3$  for E-class welding design.  $\Delta\sigma_{eq} = \sqrt[3]{\frac{\sum \Delta\sigma_i^3 \times n_i}{\sum n_i}}$  denotes the equivalent stress range, where

396  $\Delta\sigma_i$  denotes the stress range obtained in cycle  $n_i$ .

397 Further,  $n_{i-100} = ADTT_{SLi} \times \gamma_n \times 365 \times Y$  is the number of cycles corresponding to a design lifetime  
 398 of 100 years; here,  $ADTT_{SLi} = 2880$  (vehicles/day/lane) denotes the traffic volume,  $\gamma_n = 0.03$  denotes  
 399 the frequency coefficient, and  $Y = 100$  (years) denotes the design service life of the composite bridge  
 400 deck.  $N$  denotes the fatigue life in years.

401 The fatigue life prediction results at point SEL1 for different recovery ratios of tensile strength and  
 402 reloading stiffness are summarized in Table 1. The fatigue life of the OSD can be increased to a  
 403 maximum of 7.87% (from 258.9 to 279.3 years) when the self-healing recovery ratio of UHPFRC  
 404 cracks reaches 100%.

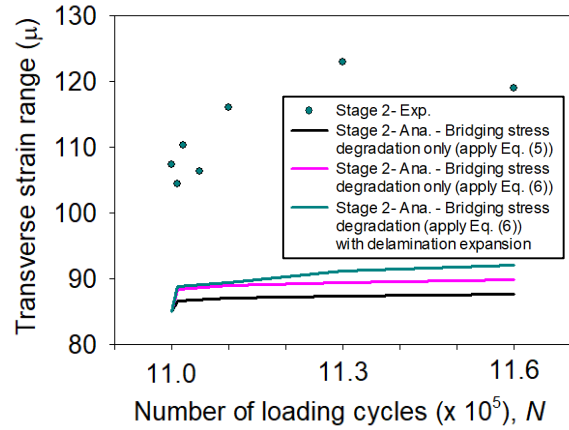
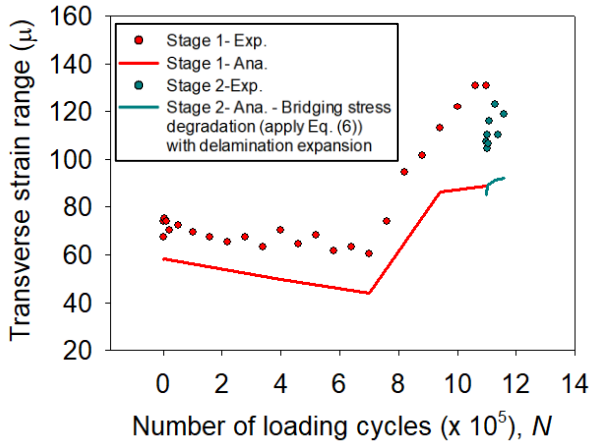
405



406

407

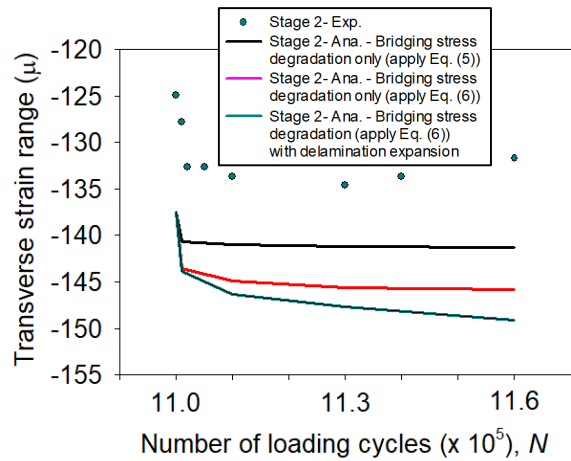
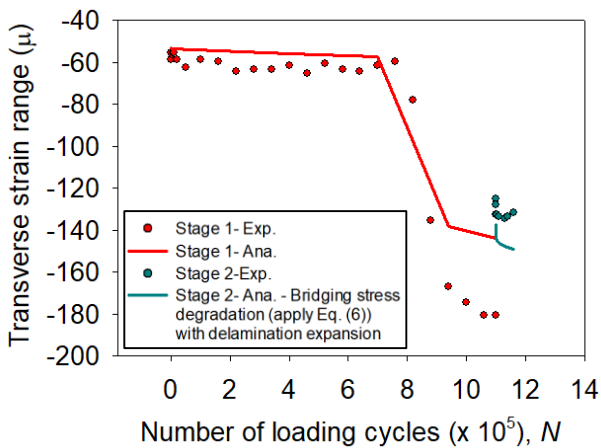
(a) SEL1



408

409

(b) SEL2



410

411

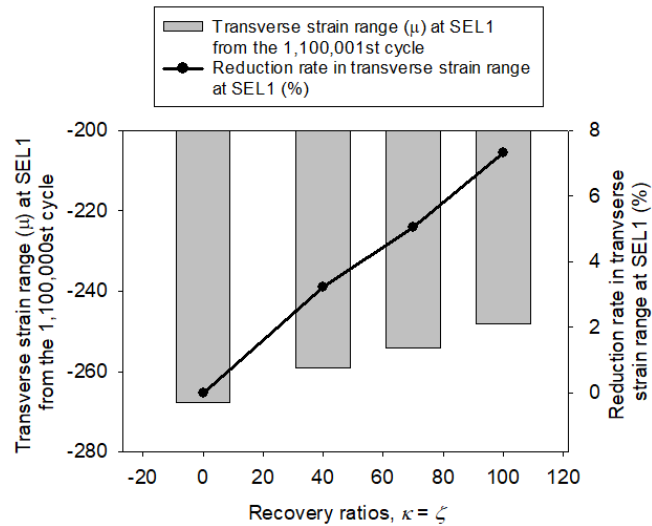
(c) SEL3

412

Fig. 10 Transverse strain range vs. the number of cycles at SEL strain gauges



413 In this self-healing phase, in the experiment with stagnant water, no material segregated on the top  
 414 surface of the UHPFRC. Such segregation can be identified based on a cloudy exudate of the  
 415 UHPFRC cracks. Fine cracks (hairline cracks) are observed on the overlayer surface at the beginning  
 416 of Stage 2 (see Fig. 16(b)). Therefore, the percentage of crack closure resulting from the self-healing  
 417 behavior is expected to be a high value after one-night exposure under the surface water condition,



418  
 419 Fig. 11 Effect of the self-healing recovery ratio on the transverse strain range at SEL1

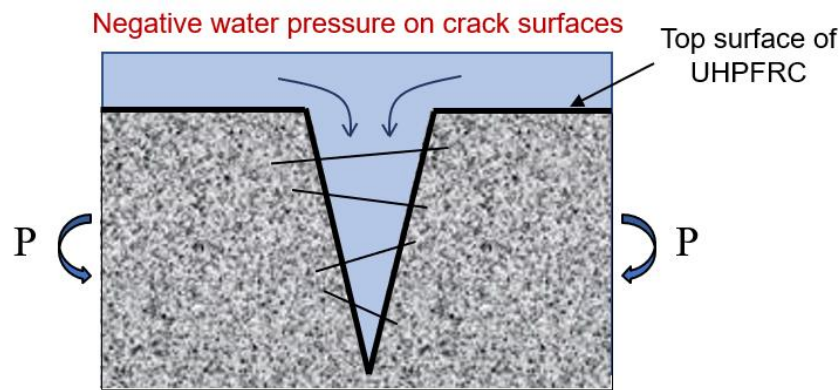
420  
 421 **Table 1.** Fatigue life prediction at a critical location of the steel deck plate

Recovery ratio (%) $\kappa = \zeta$	Equivalent stress range (MPa) $\Delta\sigma_{eq}$	Fatigue life (year) $N$	Increasing rate in fatigue life (%)
0	50.06	258.9	0
40	49.51	267.5	3.32
70	49.15	273.5	5.64
100	48.81	279.3	7.87

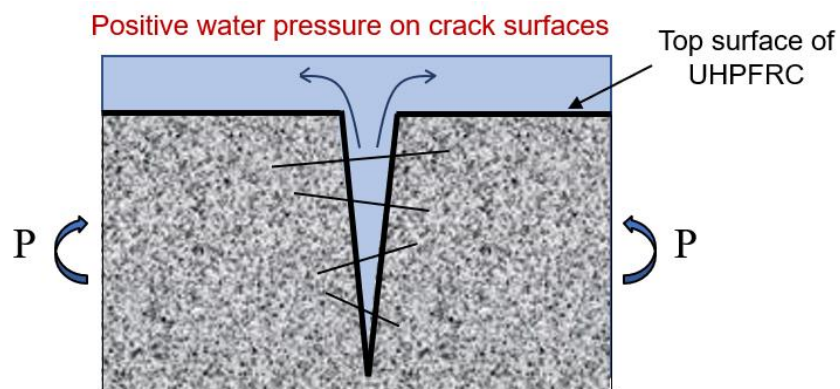
423 i.e., more than 70% based on the report for UHPFRC beams by Okuizumi et al. (2021). Following  
424 this, the recovery ratios of the tensile strength and reloading stiffness are set at values equal to the  
425 crack closure percentage and applied to the analysis.

#### 426 6.1.2.2 Effect of bridging stress degradation speed in Phase 2

427 In fatigue analysis for Phase 2, the increased speed of crack bridging stress degradation of UHPFRC  
428 is considered as shown in Eq. (6). This results in a sharp increase in steel strain levels in the initial  
429 5,000 cycles of Phase 2, as shown in Fig. 10. It is evident that the obtained results agree with the  
430 experimental data. In Figs. 10(a) and 10(c), the significant increase in the early cycles cannot be  
431 reproduced by the model using Eq. (5). Hence, it can be inferred that the increase in the bridging  
432 stress degradation speed may have occurred in the cracked UHPFRC under the moving-wheel load



(a) Crack opening in water



(b) Crack closure in water

437 Fig. 12 Water pressure generated inside a UHPFRC crack under cyclic loading

438 and surface water condition. This mechanism can be explained based on the generated water pressure  
439 inside the cracks under repetitive cyclic loading (Fig. 12). Under cyclic loading, the water pressure  
440 acting on the crack surfaces becomes negative with the opening of the UHPFRC crack. By contrast,  
441 a positive water pressure can be obtained during the closure of the UHPFRC crack in the presence of  
442 water. Hence, under the repetitive moving-wheel load, additional forces resulting from stagnant water  
443 could accelerate fatigue fiber deterioration (i.e., fiber pullout) in the fractured zone, which may result  
444 in an increase in the bridging stress degradation speed of UHPFRC cracks considered for Phase 2 of  
445 the material model of the UHPFRC.

446 From Fig. 10, it is obvious that the contribution of bridging stress degradation to the increase in  
447 the strain range is more dominant during the early stages of the fatigue analysis under the surface  
448 water condition based on a comparison between numerical models with and without interfacial  
449 delamination expansion. The reason for this is that the expansion of the debonded zone is quite  
450 minimal at the beginning cycles of Phase 2. With an increase in the number of cycles, the strain ranges  
451 of the steel plate increase, as the UHPFRC–steel composite undergoes continuous degradation when  
452 the delamination area is expanded along the transverse direction.

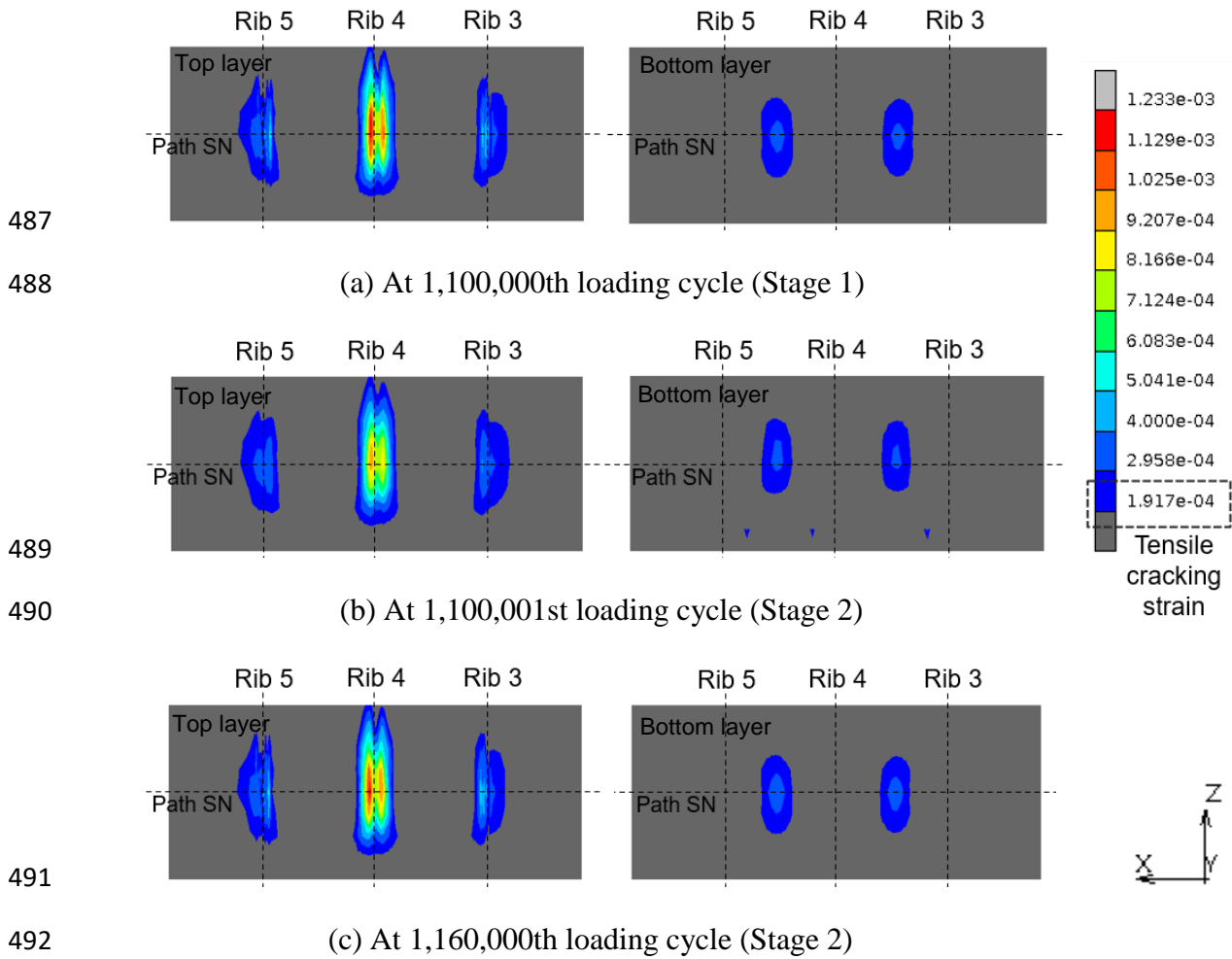
453 Overall, the qualitative agreements in strain range tendencies could be obtained from the numerical  
454 and experimental results of steel plate in the current study. Here, the proposed mechanisms for  
455 UHPFRC material model under surface water condition (i.e., the self-healing in Phase 1 and the  
456 accelerated fatigue degradation in Phase 2) are reasonable for reproducing the strain behaviors of the  
457 tested composite deck. The parametric analyses conducted in each phase have clarified the effect of  
458 each mechanism to the structural responses of steel bridge deck, as discussed above. However, from  
459 the quantitative perspective, there are still discrepancies between the analysis and the experiment.  
460 Following the research of Dai et al. (2005), it was shown that, along with the interfacial bond stiffness  
461 degradation, the residual bond slip at zero-bond stress level also increased when the number of cycles  
462 increased. Moreover, with a decrease in the tire-overlay friction coefficient owing to the presence of

463 water, the frictional force between the rubber tire and UHPFRC decreased. This may lead to  
464 additional transverse deformation at the edges of tire treads at tire contact region. Thus, in the  
465 experiment, the rubber tire contact region as well as the contact normal stresses in the surface water  
466 condition may be different from that under the dry condition. The residual bond slip at the  
467 UHPFRC/steel interface is thus affected by the contact condition of the rubber tire, i.e., in this case,  
468 the residual bond slip in the experiment may be increased. Owing to insufficient data on the current  
469 bonding technique at UHPFRC/steel interface, the residual bond strain between overlayer and steel  
470 plate under fatigue wheel loading is neglected in the current numerical model (Fig. 6(a)). This may  
471 lead to the underestimation of the unloading and reloading strain levels for the steel plate. Although  
472 experimental tendencies based on the strain range results can be relatively reproduced by the current  
473 model, the reproductions of unloading and reloading strain levels resulting from the residual bond  
474 slip at the interface, as well as the tire contact conditions in the presence of water can be considered  
475 in future studies on the composite bridge decks under moving-wheel loads.

## 476 *6.2. Numerical strain of the UHPFRC overlayer*

### 477 *6.2.1 Numerical strain distributions*

478 The maximum strain distributions for the cracked elements during Stages 1 and 2 at zone A  
479 (presented in Fig. 6(c)) are shown in Fig. 13 for the bottom and top layers of the reinforced overlayer,  
480 respectively. The blue-to-red color band represents the cracked regions on the overlayer surface. For  
481 the OSD, an overall downward movement of the steel deck plate is achieved under wheel loading,  
482 which induces positive bending at the tire contact region. However, owing to the stiffening effect of  
483 the longitudinal rib, negative bending at these local regions is produced via wheel loading. Therefore,  
484 cracks emerge on the top surface of the overlayer and propagate at local zones above Ribs 3, 4, and  
485 5; whereas tensile cracks at the bottom layer of the UHPFRC overlayer are created at the rubber-tire  
486 contact regions. At the beginning cycle of Stage 2, owing to an increase in the tensile strength caused



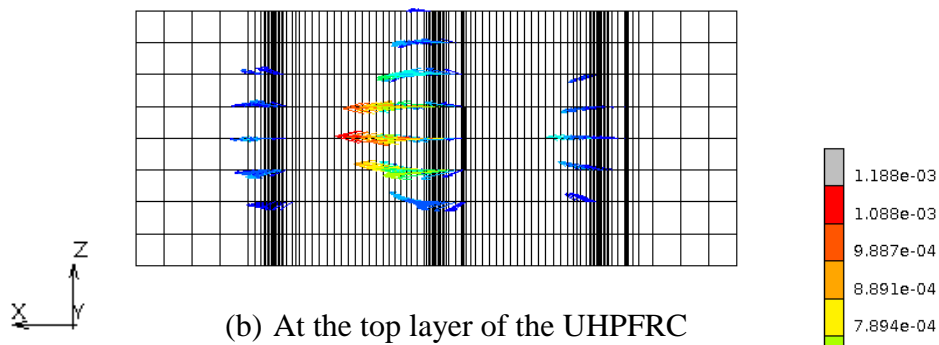
493 Fig. 13 Distributions of maximum principal strain for cracked areas on top and bottom layers of  
494 UHPFRC overlay (displayed at zone A)

495 by the self-healing of the cracks on the top layer of the UHPFRC, the maximum tensile strain levels  
496 from the top and bottom layers of the UHPFRC overlayer, as shown in Fig. 13(b), decrease compared  
497 to those under the dry condition (Fig. 13(a)). This is accompanied by a narrower crack region from  
498 the bottom layer of the overlayer. On the contrary, the maximum tensile strain level of UHPFRC  
499 increases at the end of this stage owing to a significant increase in the bridging stress degradation  
500 speed of the healed UHPFRC in stagnant water, as shown in Fig. 13(c).

501 The maximum principal strain directions obtained from the crack elements in the UHPFRC  
502 overlayer under load case 10 of the 1,160,000th cycle are depicted in Fig. 14. It is obvious that the  
503 maximum principal strain directions obtained from the crack elements on the UHPFRC top surface

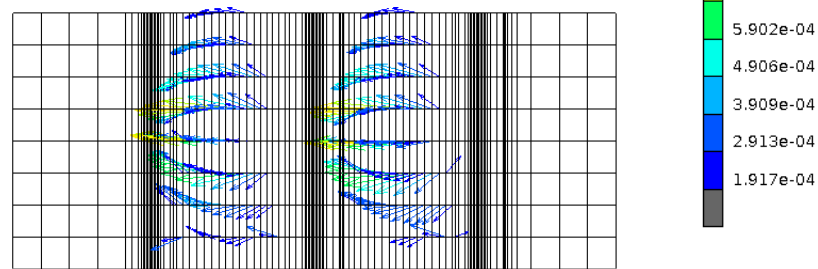
504

505



506

507



508

Fig. 14 Maximum principal strain directions of UHPFRC cracks at 1,160,000th loading cycle

509

510

511

512

513

514

515

516

517

### 6.2.2 Numerical strain evolution at the critical location of UHPFRC overlayer

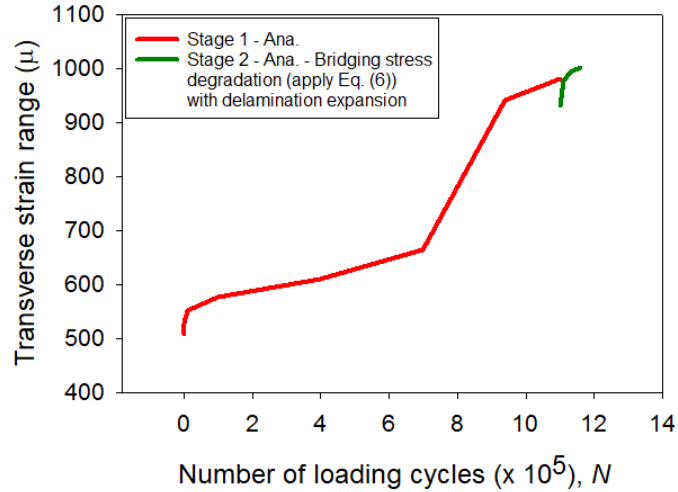
518

519

520

521

The transverse strain range evolution at the critical location on UHPFRC top surface (i.e., middle point of path SN) is plotted in Fig. 15, with the mechanical recovery ratio of 70%. Since the strain gauges separated from the UHPFRC top surface after 20,000 cycle, the discussion in this section is focused on the numerical results.



522  
523 Fig. 15 Transverse strain evolution at the middle point of path SN

524 In Stage 1, the transverse strain range of the UHPFRC overlayer gradually increase until 700,000th  
525 cycle, due to the combination of the degradations of cracked bridging stress and interfacial bond  
526 stiffness. After that, from 700,000th to 1,100,000th cycles, a considerable increase in strain range  
527 results are obtained after the formation and development of the interfacial delamination area.

528 In Phase 1 of Stage 2, it can be observed that there is a reduction in transverse strain range at the  
529 middle point of path SN in UHPFRC overlayer after applying the mechanical recovery ratios of 70%  
530 to the UHPFRC surface cracks to reproduce the self-healing behavior. Herein, the reduction  
531 percentage is approximately 5.09% (reduced from 981 $\mu$  to 932 $\mu$ ). Subsequently, under fatigue  
532 loading process (Phase 2), by applying the increased speed of crack bridging stress degradation in Eq.  
533 (6), the transverse strain results in UHPFRC overlayer continuously increase, especially from the  
534 initial 5,000 cycles of Phase 2. These results are similar to the observation of the steel strain results  
535 represented in Fig. 10.

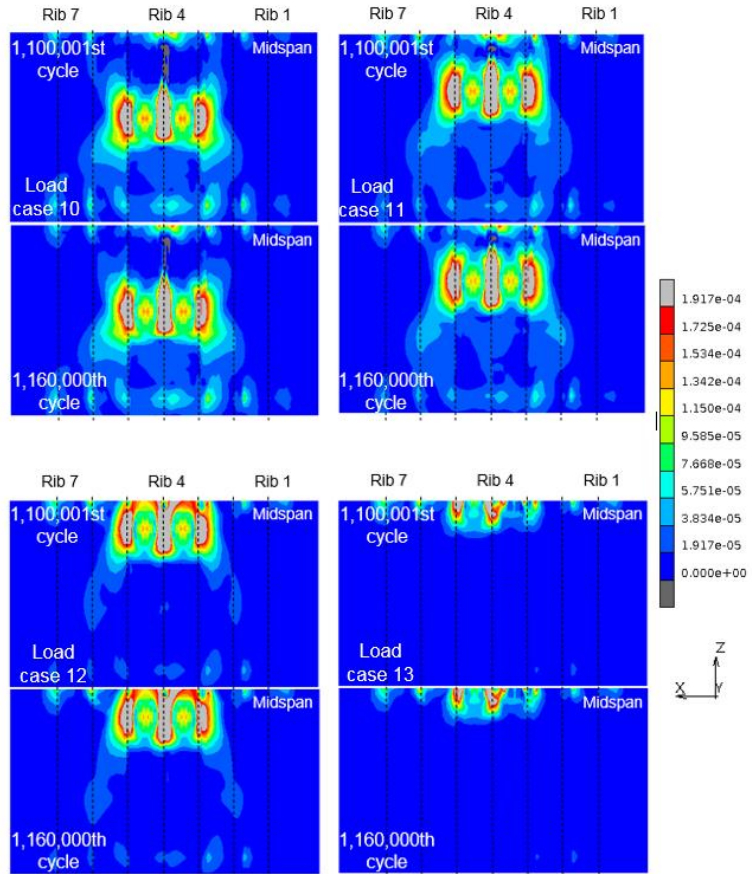
536 *6.2.3 Numerical and experimental crack region on top surface of UHPFRC*

537 Fig. 16(a) shows the distributions of the maximum principal strain from the UHPFRC top layer  
538 subjected to a moving-wheel load during the beginning and ending cycles of Stage 2. In the analysis,  
539 a sequence from load case 10 to load case 12 represents the wheel-load moving process from the east

540 patch to the center patch (Fig. 7(c)). The gray color indicates the cracked regions on overlayer surface.  
541 According to the analysis, the highest level of the maximum principal strain applied to the top layer  
542 of the UHPFRC is reported above the middle rib (Rib 4) in load case 12. In load case 13, the maximum  
543 principal strain levels and obtained cracking zone are substantially reduced compared to those in the  
544 adjacent load cases, owing to the stiffening effect of the middle crossbeam. At the end of Stage 2 with  
545 the presence of stagnant water, multiple fine cracks are not localized into macrocracks. Despite the  
546 significant increase in the bridging stress degradation speed applied for UHPFRC, the highest level  
547 of the maximum principal strain obtained from the reinforced overlayer is still within the strain-  
548 hardening domain of the UHPFRC, i.e., lower than  $1750\mu$ , at the end of Stage 2; this can be attributed  
549 to the high tensile strength, along with high fatigue durability under dry conditions for the UHPFRC.  
550 This also agrees with the surface fine cracks (hairline) observed from the experimental crack pattern  
551 shown in Fig. 16(b). Herein, it can be seen that the surface cracks occurred at the contact region of  
552 rubber tires, while no crack at this region is obtained from the analysis (Fig.16(a)). Moreover, the  
553 through-thickness cracks as well as cracks under bottom surface which were obtained in the analysis  
554 (Fig. 13) was not observed in the experiment. The possible reason for this issue may be due to the  
555 non-uniform distribution of the steel fibers in the UHPFRC overlay. As reported from the bending  
556 test of UHPFRC beams (Sakai et al., 2022), the fiber contents near the top surface of the specimens  
557 are lower than those from the bottom parts, since the fiber may sink in the matrix due to the high  
558 flowability of UHPFRC. Referring to for the current composite deck, the mechanical properties (i.e.,  
559 elastic modulus, cracking strength, tensile strength...) from the bottom layer of UHPFRC overlayer  
560 may be higher than those from the middle and top layers. Hence, further investigations of the  
561 composite bridge deck are needed to examine the effect of the non-uniformity of fiber distribution on  
562 the cracking behavior of the UHPFRC overlayer.

563 Generally, in Stage 2, the fatigue deterioration of the tested composite bridge deck is dominated  
564 by the bridging stress degradation of fractured UHPFRC on the overlayer surface. Therefore, the



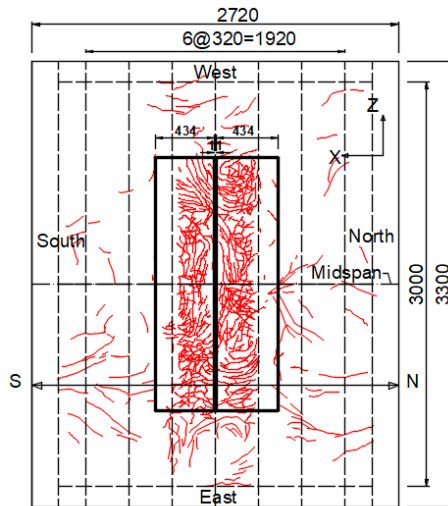


565

566

567

(a) Distributions of maximum principal strain on the UHPFRC top layer obtained from the fatigue analysis (Gray color: the crack region)



568

569

570

(b) Experimental crack pattern on UHPFRC top surface

Fig. 16 Crack region obtained from: (a) Fatigue analysis; (b) Experiment.

571 development of the crack region on the top layer of the UHPFRC, which is mainly governed by  
572 interfacial degradation, is insignificant throughout this stage owing to the small expansion of the  
573 debonded region.

## 574 **7. Conclusions**

575 In this study, a 3D nonlinear FEM analysis was performed to examine the fatigue performance of  
576 an OSD reinforced by UHPFRC overlayer under wheel loading and surface water conditions. Two  
577 phases of the material model considering the self-healing behavior and reduction in the fatigue life  
578 of UHPFRC were introduced in the numerical model. Following this, the considered mechanisms for  
579 the material model of cracked UHPFRC were assessed by investigating the UHPFRC cracking  
580 behavior and strain range of the steel deck plate based on the fatigue analysis. The following  
581 conclusions can be drawn:

- 582 (1) The efficient FE calculation which minimize the number of elements as well as the analysis  
583 time was proposed, in which the non-uniform distributions along the longitudinal and  
584 transverse directions of contact patch of rubber tire was applied for better estimations of  
585 critical responses in steel plate and overlayer.
- 586 (2) Under surface water condition, the mechanical recoveries of the tensile strength and reloading  
587 stiffness caused by the self-healing behavior can result in the reductions in strain ranges of  
588 the UHPFRC overlayer and steel plate. It was found in the analysis that the strain range at  
589 steel-plate critical location could reduce up to 7.32% with the self-healing recovery ratios of  
590 100% applied for the UHPFRC surface cracks. Correspondingly, the fatigue life of the OSD  
591 could be extended to a maximum of 7.87% in surface water condition.
- 592 (3) The effect of self-healing on reducing steel strain ranges were more apparent at the three-  
593 middle longitudinal ribs where most of UHPFRC surface cracks are located.

594 (4) Under combined condition of fatigue wheel loading and surface water, the deterioration of  
595 the UHPFRC cracks could be accelerated. By considering the reduction rate from the fatigue  
596 life of the concrete material under water condition (i.e. about 70%) to that of the UHPFRC,  
597 the degradation relation in bridging stress for UHPFRC cracks under the surface water  
598 condition was firstly introduced and applied in the current analysis.

599 (5) In Stage 2, the fatigue deterioration of the tested composite bridge deck is dominated by the  
600 bridging stress degradation of fractured UHPFRC on the overlayer surface.

601 Overall, although there were still discrepancies between the numerical and experimental strain range  
602 levels, the proposed mechanisms in the UHPFRC material model could provide a qualitative  
603 agreement in terms of strain range tendencies between the analysis and experiment. Therefore, it can  
604 be inferred that the proposed behaviors, i.e., self-healing and fatigue life reduction, are reasonable  
605 and possible to be considered in the future numerical researches of the OSD reinforced by UHPFRC  
606 overlayer under surface water condition.

607 To improve the numerical modelling of the OSD-UHPFRC composite structure, some  
608 recommendations for the future research are as follows:

609 (1) It is suggested that more fatigue tests of the OSD overlaid by UHPFRC under surface water  
610 condition are necessary to be conducted in the future to construct more experimental data for  
611 more understanding about the fatigue behavior of the UHPFRC-OSD composite structure  
612 under surface water condition, as well as for more reliable validation of the future numerical  
613 model.

614 (2) The static and fatigue shear bond test should be carried out for the epoxy bond technique to  
615 investigate the fatigue characteristic of the used epoxy-bond technique, i.e., residual bond slip  
616 caused by the bond stiffness degradation.

617 (3) The effect of the material properties of UHPFRC material, i.e., elastic modulus, tensile  
618 strength, non-uniform properties from top and bottom layers, etc., on the cracking behaviors  
619 of the UHPFRC overlayer should be further investigated.

620 (4) The tire contact conditions in the presence of water should be considered in future studies.

## 621 **Acknowledgement**

622 The current study in this paper is financially supported by a Research Grant funded by the Kajima  
623 Foundation. Besides, the J-THICOM Construction Association also provides the technical assistance  
624 for this work. This is gratefully acknowledged by the authors.

## 625 **Declaration of conflicting interests**

626 The authors declare that there is no conflict of interest.

## 627 **References**

628 Cuenca E and Serna P (2021) Autogenous self-healing capacity of early-age Ultra-High-  
629 Performance Fiber-Reinforced Concrete. *Sustainability*, 13, 3061.

630 Dai J, Saito Y, Ueda T and Sato Y (2005) Static and fatigue bond characteristics of interfaces  
631 between CFRP sheets and frost damage experienced concrete. In: *Proceedings of the Fourth*  
632 *International Symposium on Fiber Reinforced Polymer Reinforcement for Reinforced Concrete*  
633 *Structures (FRPRCS-7)*, Missouri, p. 1515-1530.

634 Deng P and Matsumoto T (2018) Determination of dominant degradation mechanisms of RC  
635 bridge deck slabs under cyclic moving loads. *International Journal of Fatigue* 112:328-340.

636 Deng P, Kaminishi H, Gouda Y and Matsumoto T (2021) Influence of insufficient early-age  
637 strength of UHPFRC on rehabilitation of OSDs. In: *Proceedings of the 10<sup>th</sup> International Conference*  
638 *on Bridge Maintenance, safety and Management*, Sapporo, Japan, 11-18 April.

639 Deng P, Mi H, Mitamura H and Matsumoto T (2022) Stress reduction effects of ultra-high  
640 performance fiber reinforced concrete overlaid steel bridge deck developed with a new interfacial  
641 bond method. *Construction and Building Materials*, 328, 127104.

642 Dieng L, Marchand P, Gomes F, Tessier C and Toutlemonde F (2013) Use of UHPFRC overlay  
643 to reduce stresses in orthotropic steel decks. *Journal of Constructional Steel Research* 89: 30-41.

644 Fairbairn EMR, Toledo Filho RD, Battista RC, Brandao JH, Rosa JI and Formagini S (2006)  
645 Experimental and numerical analysis of UHPFRC plates and shells. In: *Symposium of Measuring,  
646 Monitoring and Modeling Concrete Properties, Proceedings of the 16<sup>th</sup> European Conference of  
647 Fracture (ECF16)*, Greece, July 3-7, p. 49-58.

648 Herbert EN and Li VC (2012) Self-healing of Engineered Cementitious Composites in the Natural  
649 Environment. In: *G.J. Parra-Montesinos, H.W. Reinhardt, and A.E. Naaman (Eds.): HPFRCC 6,  
650 RILEM* p.155-162.

651 Herbert EN and Li VC (2013) Self-healing of microcracks in Engineered Cementitious  
652 Composites (ECC) under a natural environment. *Materials* 6: 2831-2845.

653 Japan Society of Civil Engineers (2008) Recommendations for Design and Construction of High  
654 Performance Fiber Reinforced Cement Composites with Multiple Fine Cracks (HPFRCC). Publisher:  
655 Concrete Committee, Japan Society of Civil Engineers.

656 Japan Society of Steel Construction (1993) Fatigue design guidelines for steel structures.

657 Jimi H, Deng P and Matsumoto T (2021) Bridging stress degradation model of UHPFRC from  
658 numerically fitting fatigue flexural test results using FEA. In: *Proceedings of the JSCE Conference  
659 Hokkaido branch No. 77, A-46*, Japan, January 30 - February 5.

660 J-THIFCOM Construction Association (2020) The material pamphlet of J-THIFCOM (Japan –  
661 Thixotropic Hardening Impermeable Fiber Reinforced Composite). Available at: [https://www.j-](https://www.j-thifcom.com/tech.html)  
662 [thifcom.com/tech.html](https://www.j-thifcom.com/tech.html).

663 Kan LL and Shi HS (2012) Investigation of self-healing behavior of Engineered Cementitious  
664 Composites (ECC) materials. *Construction and Building Materials*, 29: 348-356.

665 Kim S, Yoo DY, Kim MJ and Banthia N (2019) Self-healing capability of ultra-high-performance  
666 fiber-reinforced concrete after exposure to cryogenic temperature. *Cement and Concrete Composites*,  
667 104, 103335.

668 Li M and Li VC (2011) Cracking and healing of Engineered Cementitious Composites under  
669 Chloride environment. *ACI Materials Journal*, 108(3).

670 Li VC and Matsumoto T (1998) Fatigue crack growth analysis of fiber reinforced concrete with  
671 effect of interfacial bond degradation, *Cement and Concrete Composites* 20(5):339-351.

672 Ma CH, Deng P, Matsumoto T (2021) Fatigue analysis of a UHPFRC-OSD composite structure  
673 considering crack bridging and interfacial bond stiffness degradations. *Engineering Structures*, 249,  
674 113330.

675 Ma CH, Deng P, Ueda K, Mitamura H, Matsumoto T (2021) Finite element analysis on  
676 strengthening effect of the UHPFRC-steel composite deck. In: *Proceedings of the 10<sup>th</sup> International*  
677 *Conference on Bridge Maintenance, safety and Management*, Sapporo, Japan, 11-18 April.

678 Maekawa K and Fujiyama C (2013) Crack water interaction and fatigue life assessment of RC  
679 bridge decks. In: *Proceedings of the Poromechanics V: American Society of Civil Engineers*, Vienna,  
680 Austria, 10-12 July.

681 Makino D, Gouda Y, Mitamura H and Matsui S (2021) Wheel-load-running fatigue test of an  
682 UHPFRC-steel composite bridge deck. In: *Proceedings of the 10<sup>th</sup> International Conference on*  
683 *Bridge Maintenance, safety and Management*, Sapporo, Japan, 11-18 April.

684 Matsui S (1987) Fatigue strength of RC-slabs of highway bridge by wheel running machine and  
685 influence of water on fatigue. In: *Proceedings of Japan Concrete Institute*, 9(2): 627-632, Japan.

686 Matsui S (1996) Lifetime prediction of bridge. *Journal of Japan Society of Civil Engineers* 30:  
687 432–440.

688 Matsumoto T and Li VC (1999) Fatigue life analysis of fiber reinforced concrete with a fracture  
689 mechanics based model. *Cement and Concrete Composites* 21(4):249-261.

690 Matsushita H (1980) A study on compressive fatigue strength of concrete in the water. In:  
691 *Proceedings of the Japan Society of Civil Engineers*, JSCE, 296: 87-95.

692 Matsushita H and Tokumitsu Y (1979) A study on compressive fatigue strength of concrete  
693 considered survival probability. *Journal of Materials, Concrete Structures and Pavement, Japan*  
694 *Society of Civil Engineers* 284: 127-138.

695 Mi H (2020) *Finite element analysis on the stress reduction effects of UHPFRC overlaid steel*  
696 *bridge deck developed with a new interfacial bond method*. Master Thesis, Hokkaido University,  
697 Hokkaido, Japan.

698 Mitamura H, Omote S and Nishi H (2011) Effects of Retrofit with Two CFRP Materials of  
699 Different Properties on Fatigue Durability Improvement of RC Slabs. In: *Civil Engineering Research*  
700 *Institute (CERI) Monthly Report*, Japan, p. 2-14.

701 Okuizumi T, Deng P and Matsumoto T (2021) Experimental study about the effects of crack self-  
702 healing in UHPFRC on bending behaviors. In: *Proceedings of the JSCE Conference Hokkaido branch*  
703 *No. 77, A-20*, Japan, February.

704 Rots JG and Blaauwendraad J (1989) Crack models for concrete: discrete or smeared? Fixed,  
705 multi-directional or rotating? *HERON* 34(1):1-59.

706 Sakai R, Deng P and Matsumoto T (2022) Evaluation of fiber dispersibility of UHPFRC by X-ray  
707 CT scan and image analysis. In: *Proceedings of the JSCE Conference Hokkaido branch No. 78, A-*  
708 *16, Japan, January 29 - 30, 2022.*

709 Solwik V and Saouma EV (2000) Water pressure in propagating concrete cracks. *Journal of*  
710 *Structural Engineering* 126(2): 235-242.

711 Suthiwarapirak P, Matsumoto T and Kanda T (2004) Multiple cracking and fiber bridging  
712 characteristics of Engineered Cementitious Composites under fatigue flexure. *Journal of Materials*  
713 *in Civil Engineering*, American Society of Civil Engineers, 16(5).

714 Waagaard K (1982) Fatigue strength evaluation of offshore concrete structures. *American*  
715 *Concrete Institute, Symposium Paper 75: 373-397.*

716 Zhang J, Stang H and Li VC (1999) Fatigue life prediction of fiber reinforced concrete under  
717 flexural load. *International Journal of Fatigue* 21(10):1033-1049.

718 Zhang J, Stang H and Li VC (2000) Experimental study on crack bridging in FRC under uniaxial  
719 fatigue tension. *J Mater Civ Eng (ASCE)* 2000; 12(1):66-73.

720 Zhang Z and Zhang Q (2017) Self-healing ability of Engineered Cementitious Composites (ECC)  
721 under different exposure environments. *Construction and Building Materials*, 156: 142-151.

722